

Compton Scattering with a ^{137}Cs source

Lei Katherine, Fortin Clément, Amar Selim

McGill University Department of Physics

Supervisor: Professor Dominic Ryan, Professor Peter Grütter

February 19, 2022

Abstract

Compton scattering is used to measure the rest mass energy of the electron, to compare classical and relativistic quantum predictions for the cross section and to estimate the mass densities of Al and Cu. The radioactive sources ^{133}Ba , ^{57}Co , ^{22}Na and ^{137}Cs are used to calibrate our detector and a linear relationship between energy and our MCA's channels is found. The values obtained are $m_e c^2 = 531.4 \begin{smallmatrix} +0.3 \\ -0.3 \end{smallmatrix}$ (statistical) $\begin{smallmatrix} +15 \\ -10 \end{smallmatrix}$ (systematic) keV for the electron rest mass energy, and $\rho_{Al} = 1.8 \begin{smallmatrix} +0.3 \\ -0.3 \end{smallmatrix}$ (statistical) $\begin{smallmatrix} +0.3 \\ -0.1 \end{smallmatrix}$ (systematic) g/ml and $\rho_{Cu} = 4.8 \begin{smallmatrix} +0.3 \\ -0.3 \end{smallmatrix}$ (statistical) $\begin{smallmatrix} +0.1 \\ -0.1 \end{smallmatrix}$ (systematic) g/ml for the mass densities of Al and Cu. The relativistic quantum prediction of Klein-Nishina for the cross section is also found to be more accurate than Thomson's classical one.

Contents

1	Introduction	1
2	Apparatus and Calibration	2
2.1	Equipment and Setup	2
2.2	Calibration	3
3	Results	5
3.1	Scattering and Background Data	5
3.2	Measurement of the Electron's Rest Mass Energy	6
3.3	Measurement of the Mass Density of Al and Cu	8
4	Conclusion	10
5	Response to Comments	11

1 Introduction

The “Compton’s equation” in eq. (1) describes the shift in wavelength $\Delta\lambda$ as a function of the scattering angle θ of a photon when it is scattered by free electrons initially at rest ¹

$$\Delta\lambda = \lambda' - \lambda = \frac{h}{m_e c}(1 - \cos \theta), \quad (1)$$

where m_e is the mass of the electron and $\frac{h}{m_e c}$ the Compton wavelength. From eq. (1) and the photon’s initial energy $\gamma_i = hc/\lambda$, we can get the scattered photon’s energy γ_f by

$$\gamma_f = \frac{\gamma_i}{1 + \frac{\gamma_i}{m_e c^2}(1 - \cos \theta)}. \quad (2)$$

Fitting for the value of $m_e c^2$ is the first objective of this experiment. Furthermore, the total detection rate of photons scattered by N electrons is equal to $NI\Delta\sigma$ where I is the incident beam intensity and $\Delta\sigma$ is the electron cross section for Compton scattering. Classical and relativistic quantum theoretical results of $\Delta\sigma$ are given by Thomson and Klein-Nishina equations respectively, as functions of the detector’s solid angle $\Delta\Omega$, the scattering angle θ and fundamental constants. The classical Thomson prediction is

$$\Delta\sigma_T = \frac{1}{2}r_0^2(1 + \cos \theta)\Delta\Omega, \quad (3)$$

where $r_0 = 2.818 \times 10^{-15}$ m is the classical electron radius. Relativistic quantum considerations give the corrected Klein-Nishina cross section

$$\Delta\sigma_{K-N} = \frac{\Delta\sigma_T}{(1 + \alpha(1 - \cos \theta))^2} \left(1 + \frac{\alpha^2(1 - \cos \theta)^2}{(1 + \cos^2 \theta)(1 + \alpha(1 - \cos \theta))} \right), \quad (4)$$

with $\alpha = \frac{\gamma_i}{m_e c^2}$. By measuring the photon detection rate, we compare the two theoretical predictions to see which is more accurate, and we use the fits with fixed values for I and $\Delta\Omega$ to extract a value for the mass density of the scattering materials. These are the second and third objectives for this experiment.

¹In practice, it is only necessary that the kinetic and binding energies of the electrons are negligible compared to that of the incoming photon.

2 Apparatus and Calibration

2.1 Equipment and Setup

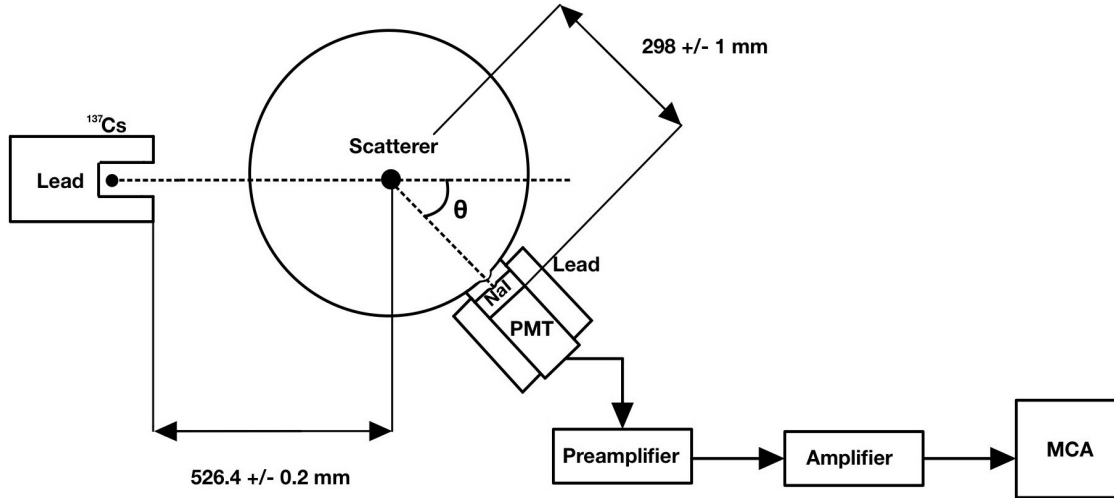


Figure 1: A schematic diagram of the experimental arrangement for measuring the Compton scattering of ^{137}Cs gamma rays from scattering targets, comprising a ^{137}Cs source of 661.6 keV gamma rays, lead shields, interchangeable scattering rod, a detection circuit comprising a NaI(Tl) scintillating crystal (Bicron [1]) on a rotating arm coupled to a photomultiplier tube (PMT) (Ortec 459 [2]) biased at V_{bias} , a preamplifier (Ortec 113 [3]), a pulse shaping amplifier (Canberra 816 [4]), and a multichannel analyzer (MCA, Ortec Easy-MCA-2k [5]). To do the calibration, radioactive sources are placed at the location of the scatterer and the strong ^{137}Cs source is blocked.

Figure 1 shows a schematic diagram of our apparatus used to measure the photons' energies. A NaI(Tl) scintillating crystal is positioned at an angle θ away from the line connecting the Cs-137 source and the scattering rod. When the gamma ray hits the crystal, it produces an amount of photons proportional to its energy. Some of them then come in contact with the active surface of the PMT and produce electrons through the photoelectric effect. The PMT amplifies these electrons into a discernible current pulse converted to a voltage pulse by the preamplifier, and then further amplified and shaped by the amplifier. Lastly, the MCA maps the peak voltage onto one of the 2048 channels available. As all the other previous processes are (approximatively) linear in their input, the MCA maps the peak voltage to a channel linearly in order for the relationship between energy and channel to come out (approximatively) linear. A zero-intercept in the MCA is also used to avoid having low

energy photons being mapped to channels outside of the range [0,2048]. Finally, due to the random variation in the number of scintillated photons produced by the crystal once a photon hits it ², the peaks are broaden into Gaussian distributions. The right panel of fig. 2 shows an example of a 30 seconds measurement for a ^{57}Co source.

2.2 Calibration

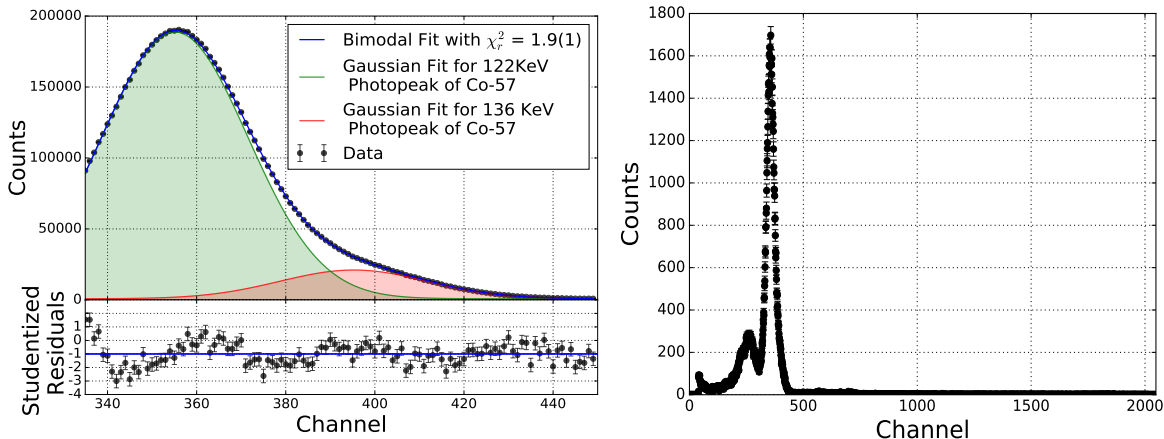


Figure 2: Left: A bimodal distribution fitted against 60 minutes of ^{57}Co data with Poisson uncertainty. Right: 30 seconds time interval of data for ^{57}Co . The highest peak includes the two photopeaks. The smaller one on its left is of unknown origin and was not used in the calibration. The left residuals in the bimodal fit exhibit structure due to the presence of this fictitious peak on their left. Fitting a third Gaussian peak did not help removing it.

To measure the scattered photons' energy, the relationship between energy and channel number need first be determined. This is done by collecting photon counts for four different sources with known gamma energy [6–9]: ^{137}Cs , ^{133}Ba , ^{57}Co and ^{22}Na . To identify peak channels, Gaussian functions are fitted using least-square methods together with a background function to filter out the noise, see section 3.1. While for most a linear background function was enough to get rid of structure in the residuals, some required a multimodal fit, given by

²The latter is actually a Poisson process but in the limit of a large number of scintillated photons (which is the case here) it approaches a Gaussian distribution.

$$f_{\text{lin}}(x) = \frac{A}{\sigma\sqrt{2\pi}} e^{-\frac{1}{2}\left(\frac{x-\mu}{\sigma}\right)^2} + Bx + C, \quad (5) \quad f_n(x) = \sum_{k=1}^n \frac{A_k}{\sigma_k\sqrt{2\pi}} e^{-\frac{1}{2}\left(\frac{x-\mu_k}{\sigma_k}\right)^2}. \quad (6)$$

For instance, the two peaks of ^{57}Co and the 31keV peak of ^{133}Ba required a bimodal fit, as shown on the left panel of fig. 2, while the 302keV and 356keV peaks of ^{133}Ba were fitted using a trimodal fit. These multimodal fits allowed us to use the small-intensity peaks of ^{57}Co at 136 keV and the one of ^{133}Ba at 302 keV in our calibrations. The bimodal fit for ^{57}Co yields a reduced chi-squared of 1.9(1), indicating good agreement with the data and justifying the inclusion of the 136 keV peak. Similar statistical goodness was found for the other fits. Further, the underlying distribution is assumed to be Poisson, yielding an uncertainty of \sqrt{N} on N counts.

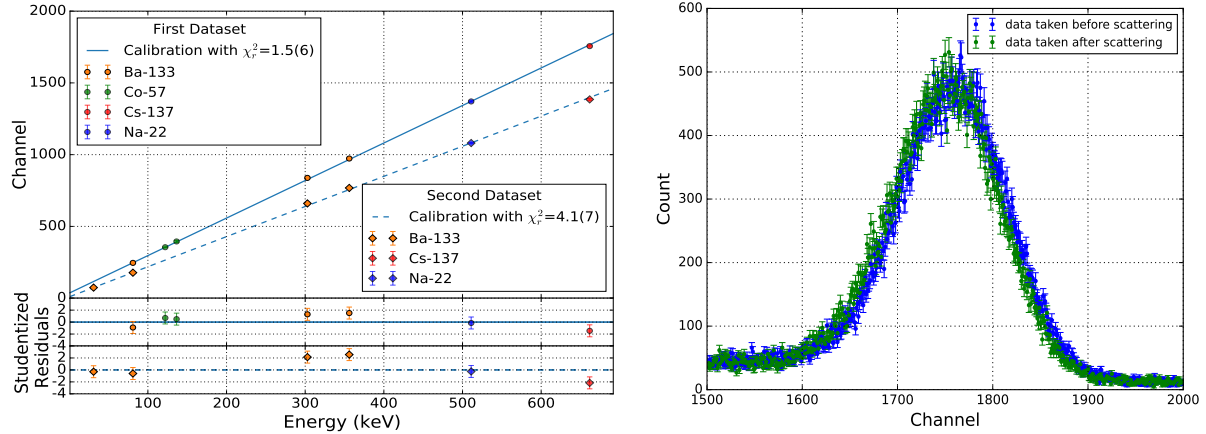


Figure 3: Left: Locations of peak channels for radioactive sources plotted against their energies. The fit parameters m and b in eq. (7) are extracted, yielding $m = 0.382(1)$ keV/channel with $b = -13.4(5)$ keV for the first dataset and $m = 0.476(1)$ keV/channel with $b = -4.3(7)$ keV for the second. Right: Shift of the ^{137}Cs peak in the first dataset when using calibration data taken before and after scattering experiments. The shift is equal to 8 channels.

For each calibrating sources, the peak channel number determined from the Gaussian fits was plotted against the corresponding energy values obtained from [6–9]. Statistical uncertainties in the peaks’ locations were obtained from the Gaussian fits while three main sources of systematic uncertainties were identified. The first one was on the order of 0.5 channel and

was estimated as the standard deviation of the distribution of peak locations we obtained when varying the channel region in which we were fitting. Furthermore, depending on which background function we used to model the noise, the location of the peak varied even though the corresponding fits had similar statistical goodness. This variation was on the order of 1 channel. The last source of systematic uncertainty is an observed shift in channel between calibration data taken before and after scattering measurements were done, as shown in fig. 3. Its contribution to the systematic uncertainty was estimated by fitting Gaussian peaks using only the ‘before’ or ‘after’ data and then setting the extreme values as our upper and lower estimates. It varied between 0.5 to 4 channels, depending on the source. Since two datasets were taken with different setups, the calibration was done separately for each of them, as shown in fig. 3. The linear function

$$ch. = f(ene.) = ene./m - b/m \quad (7)$$

is fitted to the data. The fitting parameters give the relationship $ene. = m \cdot ch. + b$ with $m = 0.382(1)$ keV/channel, $b = -13.4(5)$ keV for the first dataset and $m = 0.476(1)$ keV/channel and $b = -4.3(7)$ keV for the second one. The reduced chi-squared yield 1.5(6) and 4.1(7) respectively, indicating that these linear functions are appropriate to describe the relationship between channel and energy. The 31 keV peak of ^{133}Ba was discarded for the first dataset as it lies 10 std. away from the fit. The ^{57}Co source was not measured for the second dataset.

3 Results

3.1 Scattering and Background Data

To obtain our scattering data, we exposed aluminium and copper rods to a ^{137}Cs source of 661.657 keV gamma rays and collected the scattered photons at different angles. Two different datasets were taken: the first one consisted of 5 minutes of counts for 16 angles for both aluminium and copper, while the second one consisted of 7 minutes of counts at 15 angles for aluminium only. They were obtained at different times and using different setups, hence the analysis was done separately for both. Data with no scattering target is also

acquired at each angle in order to filter out the background signals. The latter can be due to numerous effects with two important ones being Compton scattering within the scintillator—a photon scatters in the scintillator but escapes; in that case only a fraction of its energy is deposited in the detector resulting in a Compton shelf—or Compton backscattering in the lead shielding—a photon first scatters with the lead shielding losing some of its energy. The left panel of fig. 4 is an example of the scattering data acquired for 420s with an aluminum target before and after subtracting the background data at $\theta = 26^\circ$.

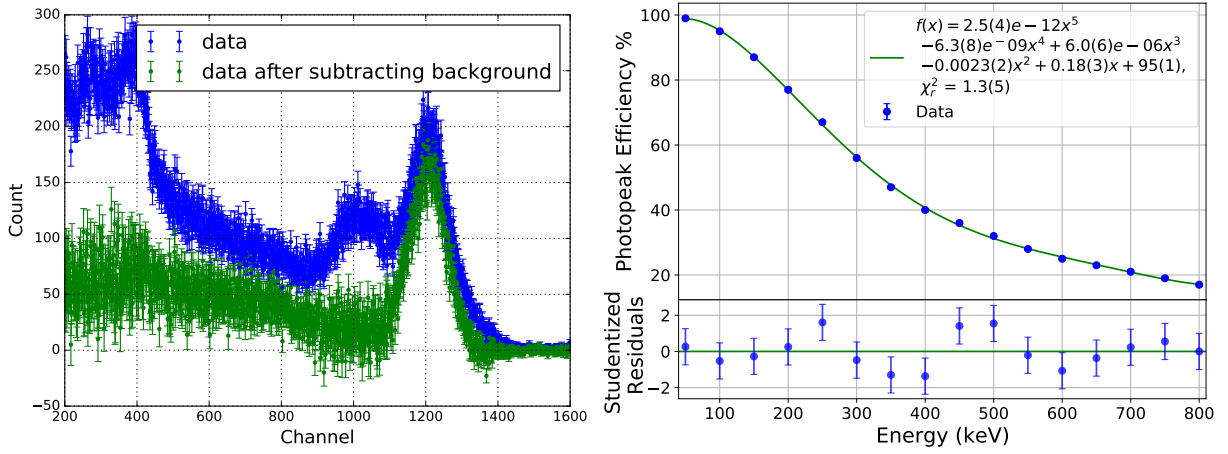


Figure 4: Left: Scattering data acquired for 420s at a scattering angle of 26° with aluminum rod, before and after subtracting the background data. The Compton shelf and backscattering peak (at $\approx 150\text{keV}$) can be observed. Right: Photopeak efficiency as a function of the energy in keV of the photon. A fifth degree polynomial is used to interpolate the data.

3.2 Measurement of the Electron's Rest Mass Energy

By fitting scattering data to eq. (2), the electron rest mass energy can be extracted. At each angle, the peak channel is found by fitting Gaussians with linear background eq. (5) to the background-subtracted data as shown on the right of fig. 5. The peak channels are converted into keV using our calibrations in section 2.2, and then eq. (2) is fitted to the resulting energy vs angle data. Both aluminium and copper rods were used to test the material dependence of eq. (2) and diminish any systematic uncertainties which we might introduce by using only one material. An offset angle θ_0 , the energy of the incoming photon γ_i and the rest mass energy of the electron $m_e c^2$ are all fitted for. In the case of aluminium, the analysis is done

for both datasets separately using the appropriate calibration and offset angles— $180.87(2)^\circ$ for the first and $163.57(3)^\circ$ for the second. The results plotted on the left of fig. 5 are given in table 1. The chi-squared values are a bit high, but the data still follows the trends.

Dataset \ Energies(keV)	$m_e c^2$	stat.	syst.	γ_i	stat.	syst.	χ_r^2
Cu+Al (1^{st})	522.4	0.5	3	654.1	0.5	2	23.8(4)
Al (2^{nd})	545.2	0.5	4	645.8	0.2	3	84.5(4)
Cu+Al (1^{st} and 2^{nd})	531.4	0.3	3	648.5	0.2	2	98.9(3)

Table 1: Fitting parameters for the Compton equation eq. (2)

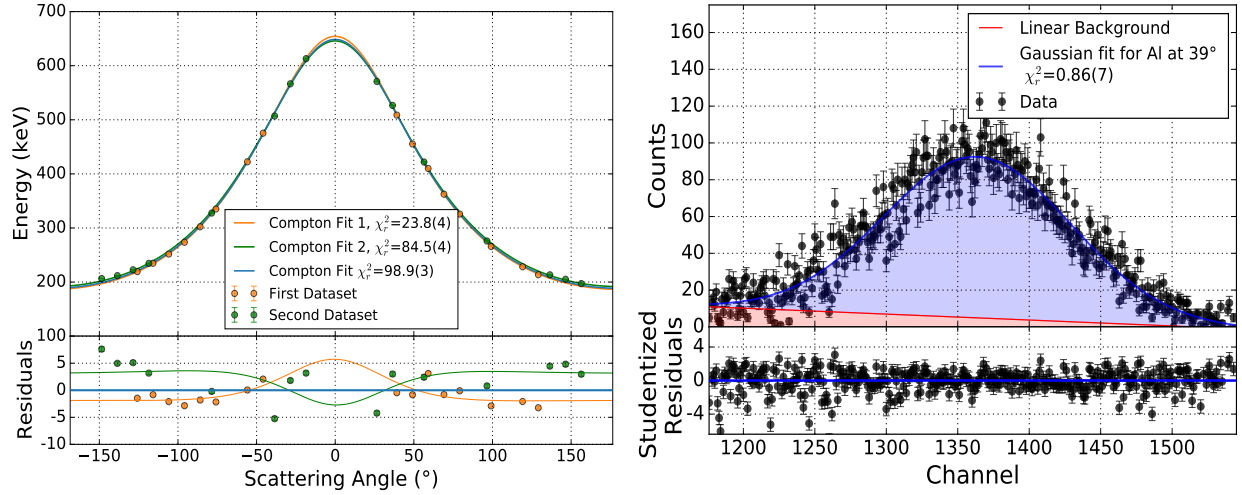


Figure 5: Left: Energy (keV) of the scattered photons versus the scattering angle with the Compton law of eq. (2) fitted. Parameter values for fits are tabulated in table 1. Right: Gaussian function with linear background fitted against the background-subtracted data at scattering angle $\theta = 39^\circ$. The blue colored region indicate the counts within the photopeak.

The systematic uncertainties above are estimated as the variation in the parameters when fitting with the extreme values of our calibrations. In the first dataset, we find the same energy for the scattered photons and for $m_e c^2$ (within statistical uncertainties) for each material, therefore it is justified to combine them and the Compton equation eq. (2) doesn't depend on these two materials. As for the second dataset, it is found to be in disagreement with the first since the values lie ≈ 5 std. away. While the reduced chi-squared of the 2^{nd} dataset is about 4 times bigger than the first, this is not enough to rule out its significance. Thus, we set our best estimate as the one of the combined datasets and included another

contribution to the systematic uncertainty as its differences with the values from each dataset. This gives us a final result of $m_e c^2 = 531.4 \pm_{-0.3}^{+0.3}(\text{statistical}) \pm_{-10}^{+15}(\text{systematic})$ keV. This value lies 2 std. away from 511 keV and is thus in slight disagreement with this literature value [10].

3.3 Measurement of the Mass Density of Al and Cu

To compare the classical and relativistic quantum predictions for the cross section, the detection rate of photons is measured for numerous angles and two scattering materials: copper and aluminium. To do so, we fitted normalized Gaussians with linear backgrounds eq. (5) to the background-subtracted data to determine the number of detected photons within the photopeaks. The latter was obtained as the amplitude A of the normalized Gaussian as on the right of fig. 5. Afterwards, we divided this count by the photopeak efficiency in order to obtain the number of scattered photons that hit the detector. In order to calculate this efficiency, we read off points from a figure provided by technicians and fitted a 5th degree polynomial to it, as shown in fig. 4. We then divided the counts by the time interval for which the data was taken to obtain the detection rate (photon/s). Finally, we fitted the Klein-Nishina prediction of eq. (4) for α , N and an offset angle θ_0 . The incident intensity I and the solid angle $\Delta\sigma$ of the detector were fixed and estimated by the formulas

$$I = \frac{I_0 \times e^{-t/(1.4427 \times \tau)}}{4\pi p_0^2} \times BF \times BR = 30330(90) \frac{\text{photons}}{s \cdot \text{cm}^2}, \quad \Delta\Omega = \pi r^2 / p_1^2 = 0.0175(1) \text{sr}, \quad (8)$$

where $I_0 = 3.7 \times 10^9$ Bq is the initial activity of the source, $t = 47.34$ years is the time elapsed since its measurement, $\tau = 30.05(8)$ years is the half-life of ^{137}Cs [11], $p_0 = 52.64(2)$ cm is the distance from the source to the target, $BF = 0.9011$ is the branching fraction for the decay, $BR = 0.944$ is the branching ratio for the photons of energy 661.657 keV, $r = 2.22$ cm is the radius of the crystal and $p_1 = 29.8(1)$ cm its distance from the target. The resulting plots, together with a fit for the Thomson prediction of eq. (3) are shown in fig. 6. We remark that the Thomson fits completely misses the behaviour of the data while the relativistic quantum predictions pass through the points with reasonable chi-squared. This demonstrates that the formula of Klein-Nishina is the one which accurately describes the cross section. The parameters of the fit obtained are presented in table 2. To combine the datasets, their offsets

angles were accounted for. Note that combining the two increases the chi-squared.

Dataset	N ($10^{24}e^-$)	stat. ($10^{24}e^-$)	syst. ($10^{24}e^-$)	α	stat.	syst.	χ_r^2
Al (1^{st})	7.7	0.8	0.2	3.5	0.6	0.1	1.4(4)
Al (2^{nd})	6.0	0.1	0.1	1.53	0.06	0.01	2.3(4)
Al (combined)	6.5	0.1	0.1	2.27	0.09	0.05	14.3(3)
Cu	16.2	1.3	0.4	4.7	0.5	0.1	4.6(4)

Table 2: Fitting parameters for the Klein-Nishina eq. (4).

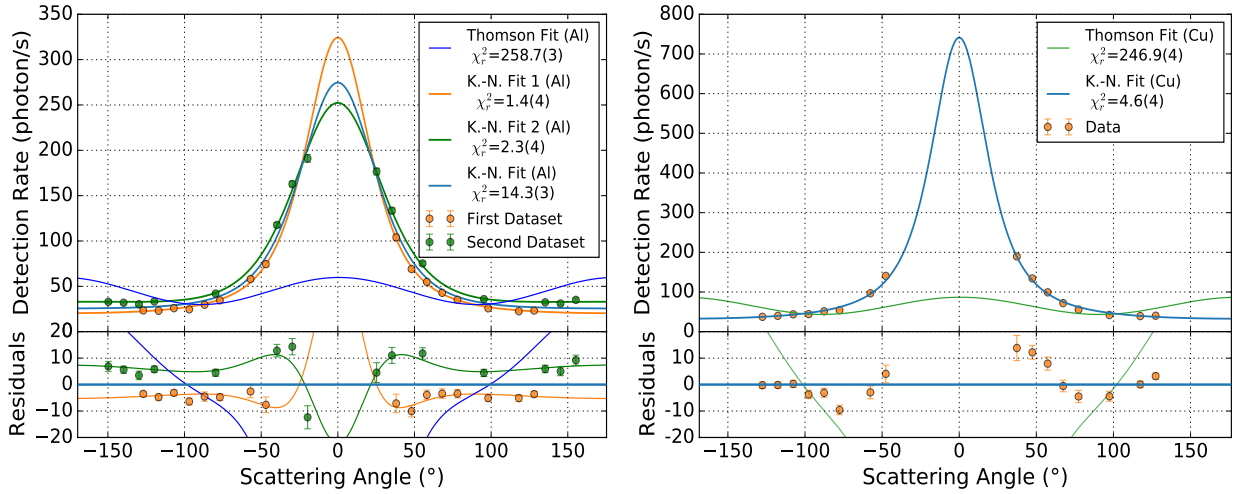


Figure 6: Left: First, second and combined dataset of photon detection rate [photon/s] as a function of scattering angle with an aluminum target. Right: Detection rate [photon/s] as a function of 16 scattering angles with a copper target. The Thomson 3 and Klein-Nishina 4 predictions are fitted for in both plots. The residual structure in copper could be reduced by obtaining additional data near 0° .

The systematic uncertainties due to the calibrations is estimated as the variation of the parameters when fitting with extreme lines of the calibration. Furthermore, for N , the uncertainties in I and $\Delta\Omega$ have also been taken into account by propagating them. In the case of aluminium, the two datasets are not in perfect agreement with each other. Since the reduced chi-squared of the two fits are both ≈ 1 , we can not determine if either one is more significant than the other. We thus use as our best estimates the parameters for both datasets combined, with upper and lower estimates given by the ones of the two datasets separately. Our best estimates are then $N_{Al} = 6.5^{+0.1}_{-0.1}$ (statistical) $^{+1.2}_{-0.5}$ (systematic) 10^{24} electrons, $N_{Cu} = 1.62^{+0.13}_{-0.13}$ (statistical) $^{+0.04}_{-0.04}$ (systematic) 10^{25} electrons and $\alpha = 2.27^{+0.09}_{-0.09}$ (statistical) $^{+1.2}_{-0.7}$

(systematic). By using that the volume of the scattering targets are $V_{Al} = 12.25(4) \text{ cm}^3$ and $V_{Cu} = 12.18(4) \text{ cm}^3$ we can then estimate the mass density of aluminium and copper. We find that $\rho_{Al} = \frac{N_{Al} \times M_{Al}}{V_{Al} \times N_A \times 13} = 1.8 \text{ }^{+0.3}_{-0.3}(\text{statistical}) \text{ }^{+0.3}_{-0.1}(\text{systematic}) \text{ g/ml}$ and $\rho_{Cu} = \frac{N_{Cu} \times M_{Cu}}{V_{Cu} \times N_A \times 29} = 4.8 \text{ }^{+0.3}_{-0.3}(\text{statistical}) \text{ }^{+0.1}_{-0.1}(\text{systematic}) \text{ g/ml}$. Here, N_A is Avogadro's constant and $M_{Al} = 26.98 \text{ g/mol}$, $M_{Cu} = 63.55 \text{ g/mol}$ are the molar masses [10, 12]. The literature values of $\rho_{Al} = 2.70 \text{ g/ml}$ and $\rho_{Cu} = 8.96 \text{ g/ml}$ [13] are 2 and 13 std. away from our results, indicating a slight disagreement for Al and a substantial one for Cu. Additional scattering data near 0° for copper could improve the accuracy for our measurement of ρ_{Cu} .

4 Conclusion

The purpose of this experiment was to 1) verify the accuracy of the Compton eq. (2) and use it to measure the rest mass energy of the electron; 2) compare the classical eq. (3) and relativistic quantum predictions of eq. (4) for the electron cross section and 3) measure the mass densities of copper and aluminium. While the measurements were not in agreement with the literature, these objectives were achieved: we obtained values of $m_e c^2 = 531.4 \text{ }^{+0.3}_{-0.3}(\text{statistical}) \text{ }^{+15}_{-10}(\text{systematic}) \text{ keV}$ (section 3.2), $\rho_{Al} = 1.8 \text{ }^{+0.3}_{-0.3}(\text{statistical}) \text{ }^{+0.3}_{-0.1}(\text{systematic}) \text{ g/ml}$ and $\rho_{Cu} = 4.8 \text{ }^{+0.3}_{-0.3}(\text{statistical}) \text{ }^{+0.1}_{-0.1}(\text{systematic}) \text{ g/ml}$ (section 3.3) for the rest mass energy of the electron and the mass densities. We also showed that the relativistic quantum prediction for the cross section in section 3.3 is the most accurate. Furthermore, our data supports the hypothesis that the Compton eq. (2) and Klein-Nishina eq. (4) describe Compton scattering since its behaviour is accurately captured by the fits. To improve this experiment, a first step would be to measure at additional scattering angles near 0° . Indeed, we only had such data for one aluminium and the only dataset in which we had such values was in disagreement with the other. These additional measurements would better define our peaks (particularly for copper) and could reduce the systematic uncertainties coming from the disagreement between the two datasets. Measuring scattering data for materials with very low or very high mass densities would be an interesting avenue to pursue, as it could determine whether the Compton equation and Klein-Nishina formula continue to hold for such extremes and if not, what are their necessary modifications.

5 Response to Comments

1. We wrote an introduction to explain the experiment and motivate the analysis.
2. We corrected our explanation for why the peaks are broaden into Gaussian. We also were clearer when explaining why the MCA has an offset.
3. We explained statistically why the 31keV peak of ^{133}Ba was removed from the calibration of the first dataset.
4. We included chi-squared values within the figures and made the labels larger. We also colored the data points differently to indicate the different sources (in the calibration) and the two different datasets.
5. We reported statistical and systematic uncertainties separately everywhere and in the right fashion. We made tables for them in order to be clearer.
6. We removed the channel versus angle fit due to the challenge of dealing with the zero-intercepts in the calibrations. Dealing with it turned out not to be worth it.
7. We clearly indicated which equations we are fitting for, numbered them and described which parameters were fitted for. In particular, we explicitly indicated that we corrected for the angle offset.
8. We described how the background data was subtracted from the scattering data and explain why this was done. Furthermore, we've added a plot comparing the raw data versus the background-subtracted data.
9. We've added a typical example of a Gaussian fit on the scattering data in order to refer to it when describing how the energy of the photons and their counts were determined.

References

- [1] Saint-Gobain Crystals. (2005) NaI(Tl) and Polyscin[®] NaI(Tl) Sodium Iodide Scintillation Material. [Online]. Available: <https://www.crystals.saint-gobain.com/sites/hps-mac3-cma-crystals/files/2021-08/Sodium-Iodide-Material-Data-Sheet.pdf> 2
- [2] Ortec. (2002) 266 Photomultiplier Base. [Online]. Available: <https://www.ortec-online.com/products/electronics/photomultiplier-tube-bases/266> 2
- [3] Ortec. (2002) 113 Scintillation Preamplifier. [Online]. Available: <https://www.ortec-online.com/products/electronics/preamplifiers/113> 2
- [4] Canberra. Spectroscopy Amplifier Model 816. [Online]. Available: http://www.nuclearphysicslab.com/npl/wp-content/uploads/Canberra_816_Spectroscopy_Amplifier.pdf 2
- [5] Ortec. (2014) Easy-MCA 2k or 8k Channel Multichannel Analyzer. [Online]. Available: <https://www.ortec-online.com/products/electronics/multichannel-analyzers-mca/basic-analog/easy-mca-2k-or-8k> 2
- [6] Y. Khazov, A. Rodionov, and F. Kondev, “Nuclear Data Sheets for A = 133,” *Nuclear Data Sheets*, vol. 112, no. 4, pp. 855–1113, 2011. [Online]. Available: <https://www.sciencedirect.com/science/article/pii/S0090375211000202> 3, 4
- [7] M. R. Bhat, “Nuclear Data Sheets for A = 57,” *Nucl. Data Sheets*, vol. 85, pp. 415–536, 1998. [Online]. Available: <https://www.sciencedirect.com/science/article/abs/pii/S0090375298900217?via%3Dihub> 3, 4
- [8] E. Browne and J. Tuli, “Nuclear Data Sheets for A = 137,” *Nuclear Data Sheets*, vol. 108, no. 10, pp. 2173–2318, 2007. [Online]. Available: <https://www.sciencedirect.com/science/article/pii/S0090375207000804> 3, 4
- [9] M. S. Basunia, “Nuclear Data Sheets for A = 22,” *Nuclear Data Sheets*, vol. 127, pp. 69–190, 2015. [Online]. Available: <https://www.sciencedirect.com/science/article/pii/S0090375215000253> 3, 4

- [10] E. Tiesinga, P. J. Mohr, D. B. Newell, and B. N. Taylor. (2018) The NIST Reference on Constants, Units and Uncertainty. [Online]. Available: https://www.physics.nist.gov/cgi-bin/cuu/Value?mec2mev|search_for=electron+mass 8, 10
- [11] R.G. Helmer and V.P. Chechev. (2007) Table de Radionucléides. [Online]. Available: http://www.lnhb.fr/nuclides/Cs-137_tables.pdf 8
- [12] NIST. (2022) NIST Chemistry WebBook. [Online]. Available: <https://doi.org/10.18434/T4D303> 10
- [13] NIST Centre for Neutron Research. (2020) Reference Table. [Online]. Available: <https://www.nist.gov/ncnr/sample-environment/sample-mounting/reference-tables> 10